crystals

MDPI

Article

Synthesis, Structure and Bonding Analysis of the Zwitterionic PPP-Pincer Complex (6-Ph_2P-Ace-5-)$_2$P(O)$AuCl_2$

Daniel Duvinage [1], Enno Lork [1], Simon Grabowsky [2], Stefan Mebs [3,*] and Jens Beckmann [1,*]

1 Institut für Anorganische Chemie und Kristallographie, Universität Bremen, Leobener Straße 7, 28359 Bremen, Germany; duvinage@uni-bremen.de (D.D.); enno.lork@uni-bremen.de (E.L.)
2 Departement für Chemie und Biochemie, Universität Bern, Freiestrasse 3, 3012 Bern, Switzerland; simon.grabowsky@dcb.unibe.ch
3 Institut für Experimentalphysik, Freie Universität Berlin, Arnimallee 14, 14195 Berlin, Germany
* Correspondence: stefan.mebs@fu-berlin.de (S.M.); j.beckmann@uni-bremen.de (J.B.)

Received: 29 May 2020; Accepted: 27 June 2020; Published: 1 July 2020

Abstract: The reaction of (6-Ph_2P-Ace-5-)$_2$P(O)H with (tht)$AuCl_3$ proceeds via elimination of tetrahydrothiophene (tht) and HCl, providing the zwitterionic PPP-pincer complex (6-Ph_2P-Ace-5-)$_2$ P(O)$AuCl_2$ (**1**) as yellow crystals. The molecular structure of **1** was established and studied by X-ray crystallography. The electronic structure was computationally analyzed using a comprehensive set of real-space bonding indicators derived from electron and electron-pair densities, providing insight into the relative contributions of covalent and non-covalent forces to the polar-covalent Au–Cl, Au–P, and P–O^- bonds; the latter being one of the textbook cases for strongly polarized covalent interactions. Partial spatial complementarity between both bonding aspects is suggested by the electronic properties of the distinctively different Au–Cl bonds.

Keywords: pincer ligands; secondary phosphine oxide; gold complex; real-space bonding indicators

1. Introduction

Recently, we introduced bis(6-diphenylphosphinoacenaphth-5-yl)phosphine oxide (6-Ph_2P-Ace-5-)$_2$P(O)H (**I**) as a novel ligand in coordination chemistry [1]. Like many other secondary phosphine oxides, **I** is in equilibrium with the corresponding phosphinous acid (6-Ph_2P-Ace-5-)$_2$POH (**I'**), from which it proved to react with nickel and palladium compounds to give a number of well-defined PPP-pincer complexes [1]. In an effort to broaden the scope of the new ligand, we have now extended our study to (tht)$AuCl_3$ (tht = tetrahydrothiophene) which yielded the metastable zwitterionic complex (6-Ph_2P-Ace-5-)$_2$P(O)$AuCl_2$ (**1**) as yellow crystals. The spatial arrangement of the Au atom was studied by means of X-ray crystallography, whereas the electronic structure was studied by density functional theory (DFT) calculations, transferring the C-H-distance corrected experimental molecular structure into the gas phase. Topological, surface, and integrated electronic bonding parameters were determined according to the Atoms-In-Molecules (AIM), [2] non-covalent interactions (NCI) [3] index, and electron localizability indicator (ELI-D) [4] methods. Real-space bonding indicators (RSBI) complement the orbital picture and extend the Lewis-picture of chemical bonding (e.g., by uncovering the vital role of weak secondary intramolecular interactions on the overall stability of complex molecules), and afford information of tiny electronic rearrangements due to structural changes. The AIM bond topology includes all types and strengths of chemical interactions and provides atomic/fragmental charges and volumes, which has made it a more routinely used tool for bonding analysis in the last three decades [5]. However, atom-atom contacts within cage structures (e.g., boranes

or metal-cyclopentadienyl complexes) or those with sharp bonding angles (e.g., intramolecular O–H ··· O) may be hidden in the electron density (ED) not giving rise to the formation of a bond critical point (bcp) [6,7]. Analysis of the reduced density gradient, $s(\mathbf{r}) = [1/2(3\pi^2)^{1/3}]|\nabla\rho|/\rho^{4/3}$, according to the NCI method, is used to visualize (extended) areas of non-covalent bonding aspects and turned out to be useful to detect contacts which are not discernible by AIM [8]. Mapping the ED times the sign of the second eigenvalue of the Hessian ($\text{sign}(\lambda_2)\rho$) on the *iso*-surfaces of $s(\mathbf{r})$ facilitates the estimation of different non-covalent contact types to be steric/repulsive ($\lambda_2 > 0$), van der Waals-like ($\lambda_2 \approx 0$), or attractive ($\lambda_2 < 0$). NCI is greatly complemented by the ELI-D, which provides electron populations and volumes of bonding and lone-pair basins and is especially suitable for the analysis of covalent bonding aspects. Notably, the combination of NCI and ELI-D (or its predecessor, ELF [9]; electron localization function) suggests the partial spatial separation of both bonding aspects [10,11]. Bond polarities are affected by the interplay between covalent and non-covalent bonding aspects and can be estimated by the intersection of ELI-D bonding basins with AIM atomic basins according to the Raub-Jansen-Index, [12] which discloses how bonding electrons are distributed over adjacent atoms forming a bond. Accordingly, the combination of AIM, NCI, and ELI-D provides a wealth of information, which is not accessible by the sole inspection of the molecular geometry or orbital-based approaches. In this study, RSBI are applied to characterize the polar-covalent Au–Cl, Au–P, and P–O^- bond types.

2. Results and Discussion

The reaction of the secondary phosphine oxide (6-Ph_2P-Ace-5-)$_2$P(O)H (**I**) [1] with (tht)$AuCl_3$ in CH_2Cl_2 at −40 °C occurred via the equilibrium of the phosphinous acid (6-Ph_2P-Ace-5-)$_2$POH (**I′**), and proceeded with the elimination of tetrahydrothiophene (tht) and HCl, and afforded the zwitterionic PPP-pincer complex (6-Ph_2P-Ace-5-)$_2$P(O)$AuCl_2$ (**1**) as yellow crystals, see Scheme 1. In solution, the stability of **1** is very limited; it decomposed within minutes at rt and within a day at −40 °C, which effectively precluded any characterization by NMR spectroscopy. The molecular structure of **1** was established by X-ray crystallography and is shown in Figure 1. Selected bond lengths are collected in the caption. The spatial arrangement of the Au(III) atom of **1** is square planar when taking into account the P_3Cl donor set of the first coordination sphere.

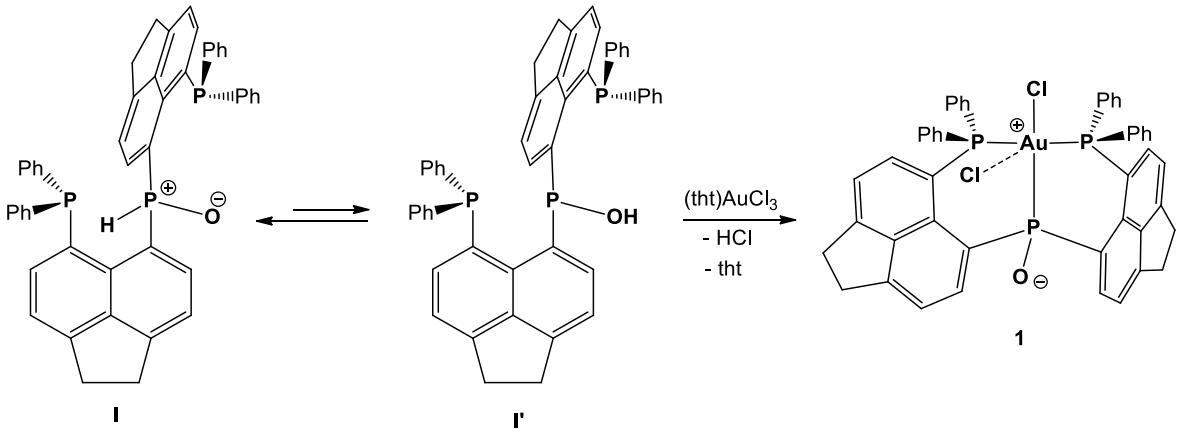

Scheme 1. Equilibrium between the secondary phosphine oxide **I** and the phosphinous acid **I′**. Synthesis of the (6-Ph_2P-Ace-5-)$_2$P(O)$AuCl_2$ (**1**).

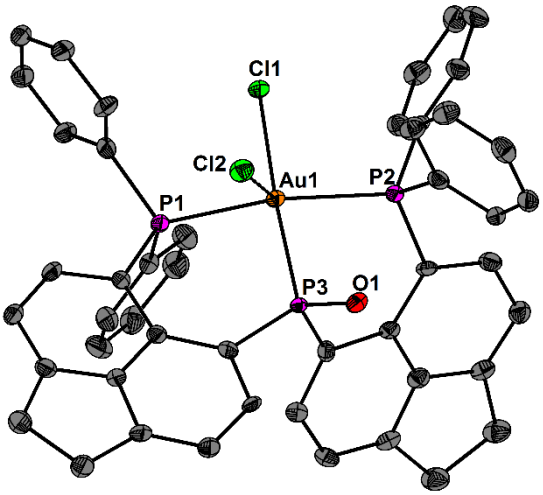

Figure 1. Molecular structure of (6-Ph_2P-Ace-5-)$_2$P(O)$AuCl_2$ (**1**) showing 50% probability ellipsoids and the essential atomic numbering. Selected bond parameters [Å,°]: Au1–P1 2.345(2), Au1–P2 2.365(1), Au1–P3 2.298(2), Au1–Cl1 2.392(2), Au1–Cl2 2.830(2), P3–O1 1.483(4), P1–Au1–P2 164.1(1), P1–Au1–P3 92.9(2), and P2–Au1–P3 82.8(2).

Considering also the second chlorine atom, the spatial arrangement can alternatively be described as distorted square pyramidal (4 + 1 coordination), as shown by the related geometry index, τ_5 ($\beta - \alpha/60°$ with $\beta = 175.2(1)°$ and $\alpha = 164.1(1)°$) = 0.185 (τ_5 is 0 for an ideal square pyramidal structure and τ_5 is 1 for an ideal trigonal bipyramidal structure) [13]. The secondary Au2···Cl2 contact (2.830(2) Å) is 0.438(2) Å longer than the primary Au-Cl bond (2.392(2) Å). The coordination of the phosphorus atoms is also asymmetric. The Au1–P1 and Au1–P2 bond lengths (2.345(2) and (2.365(1) Å) are slightly longer than the Au1–P3 bond length (2.298(2) Å) that is affected by the *trans*-effect of the Cl1 atom. The P3–O1 bond (1.483(4) Å) is very short; even shorter than those of the other two known zwitterionic complexes [(5-Ph_2P-Ace-6-)$_2$P(O)NiCl] (1.497(5) Å) and [(5-Ph_2P-Ace-6-)$_2$P(O)PdCl] (1.509(2) Å) [1].

The electronic structure of **1** was studied by DFT calculations. Figure 2a displays the AIM bond topology of **1**, showing the two primary Au–Cl and three Au–P bonds, as well as three secondary Cl···H and one Cl···C_π contact, along with all of the C–C, C–H, P–C, and P–O– bonds. The *iso*-surface representation of the NCI, however, proves the existence of additional C–H···C contact patches between the organic fragments, which do not give rise to the formation of a bond critical point (bcp), shown in Figure 2b. This points towards an additional London-dispersion stabilization of the complex. The quantitative properties at the P–O^-, Au–Cl, and Au–P bcps are given in Table 1, and those of the secondary contacts in Table 2. The AIM atomic and fragmental charges are listed in Table 3. In the strong and short P–O^- bond, covalent and non-covalent bonding aspects are both pronounced [14]. Covalent contributions are indicated by a high value for the electron density (ED, $\rho(\mathbf{r})_{bcp}$) at the P–O bcp of 1.64 e$Å^{-3}$ and a highly negative total energy density over ED ratio ($H/\rho(\mathbf{r})_{bcp}$: –0.93 a.u.). Moreover, an ELI-D bonding basin is formed, which contains 1.64e (N_{ELI}) in a volume of 2.0 $Å^{-3}$ (V_{ELI}), as seen in Figure 2c, whereas no NCI basin is formed, as shown in Figure 2d. Non-covalent contributions are indicated by a strongly positive Laplacian of the ED ($\nabla^2\rho(\mathbf{r})_{bcp}$: 29.3 e$Å^{-5}$) and a kinetic energy density over ED ratio of $G/\rho(\mathbf{r})_{bcp}$ = 2.18 a.u. With 77.8%, the Raub-Jansen-Index (RJI) is half-way between nonpolar-covalent (50–60%, e.g., C–C) and ionic or dative (>90%, e.g., Li^+F^- or N→B).

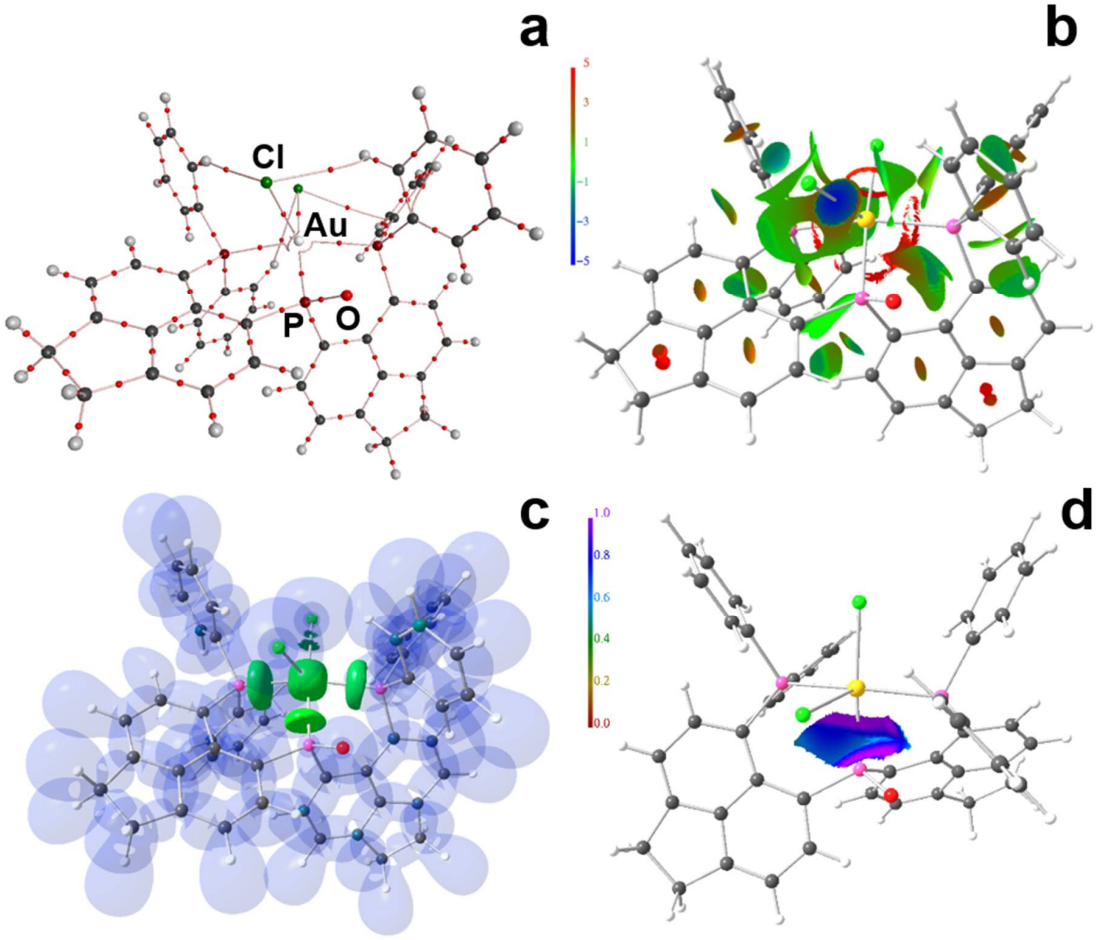

Figure 2. Real-space bonding indicator (RSBI) analysis of **1** (**a**) Atoms-In-Molecules (AIM) molecular graph, (**b**) non-covalent interactions (NCI) on the *iso*-surface at s(**r**) = 0.5 color coded with sign(λ_2)ρ (blue = attractive, red = repulsive, green = weak van der-Waals interaction), (**c**) electron localizability locator (ELI-D) localization domain representation at *iso*-value of 1.3, (**d**) ELI-D distribution mapped on the outer contour of the central P–Au ELI-D bonding basin.

The three Au–P bonds are about 0.8 Å longer, but still show the signatures of both bonding aspects, although much weaker: $\rho(\mathbf{r})_{bcp}$ is significantly below 1 eÅ^{-3} and H/$\rho(\mathbf{r})_{bcp}$ is on average −0.45 a.u., which is balanced by $\nabla^2\rho(\mathbf{r})_{bcp}$ being close to zero and G/$\rho(\mathbf{r})_{bcp}$ being about 0.5 a.u. Just like the P–O$^-$ bond, the Au–P bonds form an ELI-D but no NCI basin (disregarding the tiny ring-shaped and red-colored surfaces perpendicular to the Au–P axes). There is a trend that covalent bonding aspects are most strongly pronounced in the shortest Au–P bond (2.297 Å), for which the Laplacian already turns negative and $|H/\rho(\mathbf{r})_{bcp}| > |G/\rho(\mathbf{r})_{bcp}|$, and that ionic bonding aspects are most strongly pronounced in the longest Au–P bond (2.365 Å), for which $|G/\rho(\mathbf{r})_{bcp}| > |H/\rho(\mathbf{r})_{bcp}|$. In the even longer Au–Cl bonds (2.392 and 2.830 Å), ionic bond contributions tend to dominate: $\rho(\mathbf{r})_{bcp}$ is as small as 0.58 or 0.25 eÅ^{-3} and $|G/\rho(\mathbf{r})_{bcp}| >> |H/\rho(\mathbf{r})_{bcp}|$.

For the shorter Au–Cl bond, a tiny ELI-D basin of 0.3 e in 0.4 Å^3 is still formed (see Figure 2c), which is more polarized than the Au–P bonding basins (RJI = 82.1%), but no NCI basin is formed yet. In contrast, the longer Au–Cl bond leads to the formation of a disc-shaped and blue-colored NCI surface, which is typical for ionic bonds, as seen in Figure 2b, but no ELI-D basin is formed, supporting the spatial separation of both bonding aspects.

Table 1. Topological and integrated AIM and ELI-D properties of relevant interactions *.

Contact or Basin	d [Å]	$\rho(\mathbf{r})_{bcp}$ [eÅ^{-3}]	$\nabla^2\rho(\mathbf{r})_{bcp}$ [eÅ^{-5}]	ε	$G/\rho(\mathbf{r})_{bcp}$ [a.u.]	$H/(\mathbf{r})_{bcp}$ [a.u.]	N_{ELI} [e]	V_{ELI} [Å^3]	γ_{ELI}	RJI %
P–O	1.483	1.64	29.3	0.04	2.18	−0.93	1.64	2.0	1.56	77.8
Au–P3	2.297	0.80	−1.3	0.03	0.40	−0.51	1.67	5.1	1.68	59.4
Au–P1	2.345	0.72	1.4	0.01	0.57	−0.43	1.91	6.9	1.77	73.8
Au–P2	2.365	0.70	1.3	0.03	0.55	−0.42	1.89	6.9	1.78	73.9
Au–P	2.336	0.74	0.5	0.03	0.51	−0.45	1.83	6.3	1.74	69.0
Au–Cl1	2.392	0.58	4.2	0.02	0.82	–0.31	0.30	0.4	1.54	82.1
Au–Cl2	2.830	0.25	2.3	0.01	0.74	−0.09				

* For all bonds, d is the geometric contact distance, $\rho(\mathbf{r})_{bcp}$ is the electron density at the bond critical point (bcp), $\nabla^2\rho(\mathbf{r})_{bcp}$ is the corresponding Laplacian, ε is the bond ellipticity, $G/\rho(\mathbf{r})_{bcp}$ and $H/\rho(\mathbf{r})_{bcp}$ are the kinetic and total energy density over $\rho(\mathbf{r})_{bcp}$ ratios, N_{ELI} and V_{ELI} are electron populations and volumes of related ELI-D basins, γ_{ELI} is the ELI-D value at the attractor position, and RJI is the Raub-Jansen Index. Sorted by increasing bond distances.

Table 2. Topological AIM properties of secondary interactions *.

Contact	d [Å]	d_1+d_2 [Å]	d_t-d [Å]	d_1/d	$\rho(\mathbf{r})_{bcp}$ [eÅ^{-3}]	$\nabla^2\rho(\mathbf{r})_{bcp}$ [eÅ^{-5}]	ε	$G/\rho(\mathbf{r})_{bcp}$ [a.u.]	$H/(\mathbf{r})_{bcp}$ [a.u.]
Cl2···H73	2.476	2.478	0.002	0.65	0.11	1.1	0.02	0.62	0.12
Cl1···H88	2.901	2.928	0.027	0.63	0.05	0.5	1.53	0.60	0.14
Cl2···H34	2.905	2.921	0.017	0.61	0.05	0.6	0.10	0.62	0.15
Cl1···Cπ	3.271	3.289	0.019	0.53	0.07	0.8	3.43	0.69	0.17

* For all contacts, d is the geometric contact distance, d_1 and d_2 are the distances between atom 1 or 2 and the bcp, dt is the topological bond distance ($d_t = d_1 + d_2$), $\rho(\mathbf{r})_{bcp}$ is the electron density at the bcp, $\nabla^2\rho(\mathbf{r})_{bcp}$ is the corresponding Laplacian, ε is the bond ellipticity, and $G/\rho(\mathbf{r})_{bcp}$ and $H/\rho(\mathbf{r})_{bcp}$ are the kinetic and total energy density over $\rho(\mathbf{r})_{bcp}$ ratios. Sorted by increasing contact distances.

Table 3. AIM atomic and fragmental charges.

fragm.	Q_{001} (e)	fragm.	Q_{001} (e)
ace1	−0.94	ace2	−0.99
(ace1)Ph1	−0.38	(ace2)Ph1	−0.39
(ace1)Ph2	−0.46	(ace2)Ph2	−0.42
P1	1.80	P2	1.84
sum	*0.02*	*sum*	*0.04*
P3	2.55	Au	0.11
O	−1.45	Cl1	−0.54
		Cl2	−0.73
sum	*1.10*	*sum*	*−1.16*

Bond ellipticities are below 0.05 for all P–O$^-$, Au–Cl, and Au–P bonds, which is expected for all primary atom-atom contacts apart from contacts in ring or cage structures. The secondary Cl···H and Cl···Cπ contacts form bcps in the range from 2.48 to 3.27 Å, and follow the trend established by the primary bonds, in that they are weak and dominated by ionic bonding aspects (Table 2). The ED at the bcp is 0.1 eÅ^{-3} or smaller and $H/\rho(\mathbf{r})_{bcp}$ is already positive. These non-directed interactions are characterized by curved bond paths, resulting in a topological atom-atom distance (d_t), which is 0.002–0.03 Å longer than the geometric distance as well as bond ellipticities larger than 3 in the Cl···Cπ case. Due to the fact that **1** is zwitterionic, formally, a positive charge is situated at the gold atom and a negative charge is located at the oxygen atom. AIM finds a charge of −1.45 e for the O atom, which, however, is overcompensated by the P(–O$^-$) atom's charge of 2.55 e, resulting in a fragmental charge of 1.0 e for P–O$^-$. The Au atom is basically charge-neutral (Q = 0.11 e) and, together with the negative charges of the Cl atoms (−0.54 e for the more covalently bonded Cl1 and −0.73 e for the more ionic bonded Cl2), a fragmental charge of −1.16 e is obtained for the $AuCl_2$ moiety (Table 3). Equally strong charge separations are observed within the organic diphenyl-acenaphthyl fragments, but the overall

charges of these parts are almost zero. P atom charges typically are strongly positive and can vary largely (by about 1 e), which is less common for most other atoms, suggesting their important role in the charge-balancing processes via ligand exchange or structural modifications.

In summary, (6-Ph_2P-Ace-5-)$_2$P(O)$AuCl_2$ (**1**) is a rare example of a zwitterionic pincer compound. The series of atom-atom contacts analyzed facilitated the deconvolution between bond strength, which decreases with increasing bond distance, and bond character, which becomes more and more ionic with increasing bond distance. In this connection, the two distinctively different electronic bond properties of the Au–Cl bonds support the concept of at least partial spatial separation between covalent and non-covalent bonding aspects.

3. Experimental Section

Synthesis of **1**. In an argon-filled glovebox, bis(5-diphenylphosphinoacenaphth-6-yl)phosphine oxide [1] (100 mg, 0.138 mmol, 1.00 eq.) was dissolved in CH_2Cl_2 (5 mL) and (tht)$AuCl_3$ (54 mg, 0.138 mmol, 1.00 eq.) [15] was added. The deep red solution was immediately layered with n-hexane (2 mL) and the product crystallized at −40 °C. The product was obtained as yellow crystals, **1**·3 CH_2Cl_2, which decompose in solution at room temperature over the course of several minutes to form a gold mirror, and at −40 °C within one day.

3.1. X-ray Crystallography

Intensity data of **1**·3 CH_2Cl_2 were collected on a Bruker Venture D8 diffractometer with graphite-monochromated Mo-Kα (0.7107 Å) radiation. The structure was solved by direct methods and difference Fourier synthesis with subsequent full-matrix least-squares refinements on F^2, using all data and OLEX2 [16]. All non-hydrogen atoms were refined using anisotropic displacement parameters. Hydrogen atoms attached to carbon atoms were included in geometrically-calculated positions using a riding model. Crystal and refinement data are collected in Table 4. Figures were created using DIAMOND [17]. Crystallographic data for the structural analysis have been deposited with the Cambridge Crystallographic Data Centre, CCDC number 2005193 [18].

3.2. Computational Methodology

Density functional theory (DFT) calculations were performed for **1** in the gas phase at the B3PW91/6-311+G(2df,p) [19,20] level of theory using Gaussian09 [21]. For the Au atom, an effective core potential (ECP60MDF) and the corresponding cc-pVTZ basis set were utilized [22,23]. Only the atomic coordinates of the H atoms were optimized, whereas all other positions were kept at the XRD positions. The wavefunction files were used for a topological analysis of the electron density according to the Atoms-In-Molecules space-partitioning scheme [2] using AIM2000, [24] whereas DGRID [25] was used to generate and analyze the electron localizability indicator (ELI-D)-related [4] real-space bonding descriptors applying a grid step size of 0.05 a.u. (0.12 a.u. for visualization). The NCI [3] grids were computed with NCIplot (0.1 a.u. grids) [26]. Bond path visualizations were generated with AIM2000 and ELI-D and NCI figures were produced with MolIso [27].

Table 4. Crystal data and structure refinement.

	1·3 CH_2Cl_2
Formula	$C_{51}H_{42}AuCl_8OP_3$
Formula weight, g mol^{-1}	1244.32
Crystal system	Triclinic
Crystal size, mm	0.08 × 0.07 × 0.06
Space group	$P\bar{1}$
a, Å	11.540(5)
b, Å	11.606(5)
c, Å	21.251(5)
α, °	86.058(5)
β, °	79.833(5)
γ, °	60.908(5)
V, $Å^3$	2447.6(16)
Z	2
ρ_{calcd}, Mg m^{-3}	1.688
T, K	100
μ (Mo $K\alpha$), mm^{-1}	3.579
$F(000)$	1232
θ range, deg	2.21 to 28.59
Index ranges	$-15 \leq h \leq 15$
	$-15 \leq k \leq 15$
	$-28 \leq l \leq 28$
No. of reflns collected	116915
Completeness to θ_{max}	99.3%
No. indep. reflns	12425
No. obsd reflns with ($I>2\sigma(I)$)	10491
No. refined params	577
GooF (F^2)	1.164
R_1 (F) ($I > 2\sigma(I)$)	0.0505
wR_2 (F^2) (all data)	0.1079
$(\Delta/\sigma)_{max}$	<0.001
Largest diff peak/hole, e $Å^{-3}$	2.574/−2.984

Author Contributions: Conceptualization, J.B. and S.M.; formal analysis, E.L.; investigation, D.D.; writing—original draft preparation, J.B. and S.M.; writing—review and editing, J.B., S.M., and S.G.; visualization, J.B. and S.M.; funding acquisition, J.B. and S.G. All authors have read and agreed to the published version of the manuscript.

Funding: This research was funded by the Deutsche Forschungsgemeinschaft (DFG), grant numbers GR 4451/2-1 and BE 3716/7-1.

Acknowledgments: We are grateful to Umicore (Hanau, Germany) for a donation of precious metals.

Conflicts of Interest: The authors declare no conflict of interest.

References

1. Duvinage, D.; Puylaert, P.; Wieduwilt, E.; Malaspina, L.A.; Piltz, R.O.; Edwards, A.J.; Lork, E.; Hupf, E.; Mebs, S.; Grabowsky, S.; et al. Bis(6-diphenylphosphinoacenaphth-5-yl) phosphine oxide: A New PPP-Pincer Ligand Based upon a Secondary Phosphine Oxide (SPO). 2020 to be submitted.
2. Bader, R.W.F. *Atoms in Molecules*; A Quantum Theory; Cambridge University Press: Oxford, UK, 1991.
3. Johnson, E.R.; Keinan, S.; Mori-Sanchez, P.; Contreras-García, J.; Cohen, A.J.; Yang, W. Revealing Noncovalent Interactions. *J. Am. Chem. Soc.* **2010**, *132*, 6498–6506. [CrossRef] [PubMed]
4. Kohout, M. A Measure of Electron Localizability. *Int. J. Quantum Chem.* **2004**, *97*, 651–658. [CrossRef]
5. Stalke, D. Meaningful Structural Descriptors from Charge Density. *Chem. Eur. J.* **2011**, *17*, 9264–9278. [CrossRef] [PubMed]

6. Mebs, S.; Kalinowski, R.; Grabowsky, S.; Förster, D.; Kickbusch, R.; Justus, E.; Morgenroth, W.; Paulmann, C.; Luger, P.; Gabel, D.; et al. Real-Space Indicators for Chemical bonding. Experimental and Theoretical Electron Density Studies of Four Deltahedral Boranes. *Inorg. Chem.* **2011**, *50*, 90–103. [CrossRef] [PubMed]
7. Mebs, S.; Chilleck, M.A.; Grabowsky, S.; Braun, T. Hapticity Uncovered: Real-Space Bonding Indicators for Zincocene Chemistry. *Chem. Eur. J.* **2012**, *18*, 11647–11661. [CrossRef]
8. Lane, J.R.; Contreras-Garcia, J.; Piquemal, J.-P.; Miller, B.J.; Kjaergaard, H.G. Are Bond Critical Points Really Critical for Hydrogen Bonding? *J. Chem. Theory Comp.* **2013**, *9*, 3263–3266. [CrossRef]
9. Becke, A.D.; Edgecombe, K.E. A simple measure of electron localization in atomic and molecular systems. *J. Chem. Phys.* **1990**, *92*, 5397–5403. [CrossRef]
10. Gillet, N.; Chaudret, R.; Contreras-Garcia, J.; Yang, W.; Silvi, B.; Piquemal, J.P. Coupling Quantum Interpretative Techniques: Another look at Chemical Mechanisms in Organic Reactions. *J. Chem. Theory Comp.* **2012**, *8*, 3993–3997. [CrossRef]
11. Mebs, S. Complex modes of bonding: NCI/ELI-D vs. DORI surface analyses of hapticities and hydrogen-hydrogen contacts in zincocene related compounds. *Chem. Phys. Lett.* **2016**, *651*, 172–177. [CrossRef]
12. Raub, S.; Jansen, G.A. Quantitative Measure of Bond Polarity from the Electron Localization Function and the Theory of Atoms in Molecules. *Theor. Chem. Acc.* **2001**, *106*, 223–232. [CrossRef]
13. Addison, A.W.; Rao, N.T.; Reedijk, J.; van Rijn, J.; Verschoor, G.C. Synthesis, structure, and spectroscopic properties of copper(II) compounds containing nitrogen–sulphur donor ligands; the crystal and molecular structure of aqua[1,7-bis(N-methylbenzimidazol-2′-yl)-2,6-dithiaheptane]copper(II) perchlorate. *J. Chem. Soc. Dalton Trans.* **1984**, 1349–1356. [CrossRef]
14. Fugel, M.; Beckmann, J.; Jayatilaka, D.; Gibbs, G.V.; Grabowsky, S. A Variety of Bond Analysis Methods, One Answer? An Investigation of the Element−Oxygen Bond of Hydroxides H_n XOH. *Chem. Eur. J.* **2018**, *24*, 6248–6261. [CrossRef] [PubMed]
15. Upmann, D.; Näther, C.; Jess, I.; Jones, P.G. Four Crystalline Forms of (Tetrahydrothiophene)trichloridogold (III): Polymorphism and Reversible Low-temperature Phase Transitions. *Z. Anorg. Allg. Chem.* **2017**, *643*, 311–316. [CrossRef]
16. Dolomanov, O.V.; Bourhis, L.J.; Gildea, R.J.; Howard, A.K.; Puschmann, H. *OLEX2*: A complete structure solution, refinement and analysis program. *J. Appl. Cryst.* **2009**, *42*, 339–341. [CrossRef]
17. Brandenburg, K. *Diamond, Version 4.0.4*; Crystal Impact GbR: Bonn, Germany, 2012.
18. CCDC. Available online: http://www.ccdc.cam.ac.uk (accessed on 1 July 2020).
19. Becke, A.D. A New Mixing of Hartree-Fock and Local-Density-Functional Theories. *J. Chem. Phys.* **1993**, *98*, 5648–5652. [CrossRef]
20. Perdew, J.P.; Chevary, J.A.; Vosko, S.H.; Jackson, K.A.; Pederson, M.R.; Singh, D.J.; Fiolhais, C. Atoms, Molecules, Solids, and Surfaces: Applications of the Generalized Gradient Approximation for Exchange and Correlation. *Phys. Rev. B* **1992**, *46*, 6671–6687. [CrossRef]
21. Frisch, M.J.; Trucks, G.W.; Schlegel, H.B.; Scuseria, G.E.; Robb, M.A.; Cheeseman, J.R.; Scalmani, G.; Barone, V.; Petersson, G.A.; Nakatsuji, H.; et al. *Gaussian 16, Revision C.01*; Gaussian, Inc.: Wallingford, CT, USA, 2016.
22. Figgen, D.; Rauhut, G.; Dolg, M.; Stoll, H. Energy-consistent pseudopotentials for group 11 and 12 atoms: Adjustment to multi-configuration Dirac–Hartree–Fock data. *Chem. Phys.* **2005**, *311*, 227–244. [CrossRef]
23. Peterson, K.A.; Puzzarini, C. Systematically convergent basis sets for transition metals. II. Pseudopotential-based correlation consistent basis sets for the group 11 (Cu, Ag, Au) and 12 (Zn, Cd, Hg) elements. *Theor. Chem. Acc.* **2005**, *114*, 283–296.
24. Biegler-König, F.; Schönbohm, J.; Bayles, D. A Program to Analyze and Visualize Atoms in Molecules. *J. Comput. Chem.* **2001**, *22*, 545–559.
25. Kohout, M. *DGRID-4.6*; Springer: Radebeul, Germany, 2015.
26. Contreras-García, J.; Johnson, E.; Keinan, S.; Chaudret, R.; Piquemal, J.-P.; Beratan, D.; Yang, W. NCIPLOT: A Program for Plotting Noncovalent Interaction Regions. *J. Chem. Theor. Comp.* **2011**, *7*, 625–632. [CrossRef] [PubMed]
27. Hübschle, C.B.; Luger, P. MolIso—A Program for Colour-Mapped Iso-Surfaces. *J. Appl. Crystallogr.* **2006**, *39*, 901–904. [CrossRef]